Journal of
Materials Chemistry C

Enhanced thermoelectric performance by resonant vibrational mode-selective density-of-states distortions

Journal:	*Journal of Materials Chemistry C*
Manuscript ID	TC-COM-05-2022-001843.R2
Article Type:	Paper
Date Submitted by the Author:	23-Jun-2022
Complete List of Authors:	Birch, Shantonio; University of Michigan, Mechanical Engineering Pipe, Kevin; University of Michigan, Mechanical Engineering; University of Michigan, Electrical Engineering and Computer Science

ARTICLE TYPE

Cite this: DOI: 00.0000/xxxxxxxxxx

Enhanced thermoelectric performance by resonant vibrational mode-selective density-of-states distortions†

Shantonio W. Birch*[a] and Kevin P. Pipe[a,b]

Received Date
Accepted Date

DOI: 00.0000/xxxxxxxxxx

A method is developed that can emulate the dramatic enhancement of the thermoelectric power factor (PF) traditionally predicted to occur near the band edge of high-performance thermoelectric materials. The method uses photo-excitation of an infrared (IR)-active intramolecular vibration mode in a weakly-bonded (soft) organic material to couple high-mobility band states to tail states, creating sharply-peaked Dirac-delta-like resonant states within the tail density-of-states (DOS) that also enhance the carrier mobility (μ), the number of conducting carriers (N), and the asymmetry in the energy distribution of conducting carriers ($\sigma(E)$). The use of these resonant DOS distortions to optimize PF is explored as a function of the number of IR photons (N_{ph}). As N_{ph} is increased to augment the coupling between valence carriers and C-C stretching vibrations, a resonant four-step intramolecular charge transfer process is shown to shift the average energy of conducting carriers from band states to a position in the DOS tail near the intrinsic Fermi level. A critical photon number ($N_{ph} = 35$) is observed where DOS peaks merge to create a high mobility band of states on one side of the Fermi level and diverge to create a low mobility band of states on the other side. As a consequence, large asymmetries develop in $\sigma(E)$, causing PF to attain a maximal value when the merged high-mobility DOS peak is located $\sim 2.4k_BT$ from the Fermi level. Importantly, these DOS distortions provide improvements in PF in the DOS tail and is therefore accessible to carrier concentrations achievable by traditional doping techniques.

1 Introduction

The creation of resonant Dirac delta-like features in the electronic density of states (DOS) has long been pursued as a strategy for high thermoelectric (TE) energy conversion efficiency,[1–11] as such features provide a large asymmetry in the energy distribution of conducting carriers when the Fermi level (E_F) is located in their vicinity.[12,13] Recent methods for creating such features have included: reducing DOS dimensionality[1–4,11] and engineering resonant impurity levels,[5–10] both relying on creating perturbations within band states to enhance the thermoelectric power factor (PF).[14–16]

While prior methods have explored the creation of sharp Dirac-delta-like features among band states, such features have also been observed in DOS tails. For example, sharp tail features are known to appear in the class of weakly-bonded (soft) organic materials under both thermal (equilibrium)[17–22] and non-thermal (non-equilibrium)[23–29] conditions, and have also been routinely engineered to occur within the broader class of disordered organic and inorganic wide band gap materials[30–38] that exhibit Fermi level pinning in the DOS tail due to deep trap states (e.g., rubrene, pentacene, and amorphous silicon).[20,39–45] However, very little is known about how to take advantage of these resonant tail features for optimal power factor enhancement, even though tail features could be particularly useful for optimizing PF, since achieving sufficient carrier concentration (p) to place the Fermi level near a resonant Dirac-delta-like DOS distortion in the tail may be possible with present doping techniques,[39,46,47] while achieving sufficient levels of p needed to place E_F near a similar feature within the band may not be possible.[34,35,48,49]

Here, we adopt a well-established model for the formation of Dirac-delta-like distortions in DOS tails by the optical excitation of vibrational modes[50–56] and use it to study the thermoelectric properties of the prototypical soft organic material rubrene in the presence of infrared (IR) light that couples to valence electrons via resonant IR-active vibrational modes.[23–25,38,57,58] The results suggest that DOS distortions caused by the IR stimulation of C-C stretching vibrations in rubrene could lead to dramatic improvements in the thermoelectric PF in tail states, akin to those that result upon introducing resonant dopants to enhance PF within the band.[9,10] This resonant enhancement of PF, while induced by photo-excitation, is distinct from the photogeneration of carriers associated with Holstein small polaron formation[53–56,59] and the Photo-Seebeck effect,[60,61] and instead is shown to occur via a resonant four-step intramolecular charge transfer process that facilitates both charge delocalization and the creation of resonant DOS distortions near the intrinsic Fermi level position.

[a] Department of Mechanical Engineering, University of Michigan, Ann Arbor, MI 48109, USA; E-mail: swbirch@umich.edu
[b] Department of Electrical Engineering and Computer Science, University of Michigan, Ann Arbor, MI 48109, USA; E-mail: pipe@umich.edu

† Electronic Supplementary Information (ESI) available: ESI Notes 1-5 and Figs. S1-S5. See DOI: 00.0000/00000000.

2 Physical Model

To study the redistribution of band carriers to DOS tail states due to the mode-selective absorption of incident light, we first incorporate broadening in a model DOS to replicate the biexponential decay in the tail that is typically measured in soft organic materials[20,42,62] and disordered wide bandgap inorganic materials,[43–45] recognizing that this realistic energy dependence is particularly important for calculation of thermoelectric properties such as the Seebeck coefficient (S).[12,39,63,64] Using this DOS we then develop a framework for the non-thermal excitation of a particular vibrational mode given by the following model for an isolated vibrating molecule interacting with light in an optical cavity:[50–52,65]

$$H = H_0 + H_I. \tag{1}$$

where the unperturbed Hamiltonian H_0 is the Hamiltonian of the non-interacting material system and the interaction Hamiltonian ($H_I = H_{radia.} + H_{dipole}$), which describes the light-coupled component of the interacting material-radiation field system, is composed of the Hamiltonians of the interacting radiation field and the electric dipole moment of the radiative transition, given in the dipole approximation as:[50–52]

$$H_{radia.} = \sum_{s}^{N_s}\left(\hbar\omega_s^{(i)}\sum_j a_j^\dagger a_j + \sum_j g_{\omega_s}^{(i)} c_2^\dagger c_2 (a_j^\dagger + a_j)\right) \tag{2}$$

$$H_{dipole} = \epsilon_1 c_1^\dagger c_1 + \epsilon_2 c_2^\dagger c_2 + \sum_s^{N_s}\sum_j (M_s^{(i)*} a_j + M_s^{(i)} a_j^\dagger) \times (c_1^\dagger c_2 + c_2^\dagger c_1). \tag{3}$$

Here, ϵ_1 and ϵ_2 are respectively the ground state and excited state energies, $g_{\omega_s}^{(i)}$ is the linear coupling between the radiation field and the local electron density (i.e., $n_j = c_2^\dagger c_2$), $M_s^{(i)}$ is the electric dipole matrix element associated with the transition between the two electronic levels, $c_{1(2)}^\dagger$ and $c_{1(2)}$ are the creation and annihilation operators for a hole in electronic levels 1 and 2, $a_j^\dagger$ and a_j are the creation and annihilation operators for a phonon with transition frequency $\omega_s^{(i)} = (\epsilon_2 - \epsilon_1)/\hbar$, N_s is the total number of modes in the laser cavity associated with the modulation frequency $\omega_s^{(i)}$, the subscript s denotes the particular vibration mode that is excited, and the superscript i denotes whether or not this vibration mode is an intramolecular mode ($i = 1$) or an intermolecular mode ($i = 2$). In what follow, we only consider modulation frequencies ω_s that are tuned to the characteristic frequency of an intramolecular C-C stretching vibration $\omega_0 = 215\ meV$ (which is an optical vibration mode),[23–25,38,53,57,58] and drop the superscript i.

2.1 General Solution

The above model formulation was originally devised to assess the plasmonic[50–52,65–69] and polaronic origins[53–56,59] of resonant Dirac-delta-like peaks measured by x-ray[66] and ultraviolet angle-resolved photoemission spectroscopy (ARPES) experiments performed on metallic materials,[67] and is routinely applied in the modeling of similar features within the DOS tail of soft organic materials[26,27,29,56,62] and halide perovskites.[29] Accordingly, the general solution[68] follows from mapping the Green's function solution of the interaction Hamiltonian onto a self-consistent field of the unperturbed material's Hamiltonian defined by the following set of dynamical mean-field relations (generalized for a thermalized lattice):[50–52,54–56]

$$G\left(E'\right) = \frac{1}{Z_s}\sum_n\left(\frac{e^{-n\omega_s/k_BT}}{G_0^{-1}(E) - \Sigma_{imp}(E')}\right), \tag{4}$$

$$G\left(E'\right) = \int_{-\infty}^{+\infty} dE \frac{\hat{\rho}(E)}{E' - E_p - \Sigma_{\rm imp}(E')}, \tag{5}$$

$$\hat{\rho}(E) = -Im\ G_0(E), \quad \Sigma_{\rm imp}(E) = \Sigma'(E) - i\Sigma''(E). \tag{6}$$

Here, $Z_s = \sum_n e^{-n\omega_s/k_BT}$ is the partition function associated with the optical excitation of a C-C stretching vibration mode. $G_0(E) = (E - H_0)^{-1}$ is the Green's function for the non-interacting Hamiltonian, to which we have applied a homogeneous broadening $\Sigma''(E) = \pi\lambda k_BT/\hbar$ to replicate the biexponential decay of the DOS tail that is typically measured in soft organic materials and some amorphous wide bandgap inorganic materials ($\lambda = 0.17$ is the electron-phonon coupling associated with thermal disorder in the prototypical material rubrene).[20,42–44,62] E_p is energy of the new electronic ground state formed upon small polaron formation. $G(E')$ describes the renormalization of carriers in the highest-occupied molecular orbital (HOMO) band dispersion $A(k,E)$ (due to the dephasing of carriers brought about by IR vibrations),

$$A(\mathbf{k},E) = -\frac{1}{\pi}\,\mathrm{Im}\int d\tau c^{i\omega\tau} G_{i,j}(\mathbf{k},E,\tau,\tau_{el}), = \frac{1}{\pi}\frac{\Sigma''(E)}{[E - \zeta_{\mathbf{k}} - \Sigma'(E)]^2 + [\Sigma''(E)]^2}, \tag{7}$$

where $\Sigma''(E) = 1/2\tau_{el}$ (defined above) is recognized as the inverse lifetime broadening or the carrier dephasing time. $\Sigma'(E)$ denotes the self-energy correction to the dephasing of carriers in the HOMO dispersion due to the absorption and emission of molecular vibrations having energies that are greater than the thermal energy (i.e., $\hbar\omega_0 > k_BT$):[50–52,54–56]

$$\Sigma'^{(\pm)}(E) = \cfrac{\omega_s|M_s|^2}{G_0^{-1}(E \pm \omega_s) - \cfrac{2|g_{\omega_s}|^2}{G_0^{-1}(E \pm 2\omega_s) - \cfrac{3|g_{\omega_s}|^2}{G_0^{-1}(E \pm 3\omega_s) - ..}}}, \tag{8}$$

where the "+" superscript denotes absorptive processes, the " −" superscript denotes emissive processes, and $G_0(E \pm \omega_s)$ denotes the Green's function for the displaced cloud of polarized molecular distortions (also known as a polaron),[59] formed upon light excitation. Finally, to simulate the transfer of carriers into a higher-lying excited state and a non-equilibrium build-up of carriers

there, we invoke the following change of variable in the electric dipole matrix element term in Eq. (8): $M_s \rightarrow g_{\omega_s}\sqrt{N_{ph}+1}$,[65] where N_{ph} is the "cavity photons" or the average number of photons in the optical cavity.

2.2 Transport Relations

Starting from a representative DOS model before IR light excitation (ESI Note 1), this framework provides a relatively straightforward and reliable means for reconciling the effects of molecular vibrations on known perturbations of the electronic band structure, such as the "kink-like" feature that was recently measured at the top of the HOMO band of single crystal rubrene (ESI Note 2 and 3).[26,27,29] Thus, by simply tuning the cavity photons (N_{ph}) and modulation frequency (ω_s) to be resonant with a particular intramolecular vibration mode, Eq. (4) to (6) enable an accurate assessment of the effects of IR-activated vibrations (e.g., C-C stretching vibrations) on the dephasing of $\hat{\rho}(E)$ and A(k,E) [c.f Eq. (6) and (7)]; from these quantities all relevant TE properties, such as the DOS [given by $DOS(E) = tr\hat{\rho}(E) = \sum_k A(k,E)$] and the following transport properties:[12,63,64]

$$\sigma = \int \sigma(E,E_F)\,dE, \tag{9}$$

$$\begin{aligned} S &= -\frac{k_B}{q\sigma}\int\left(\frac{E_F-E}{k_BT}\right)\sigma(E,E_F)\,dE \\ &= -\frac{1}{qT}\left(E_{tr}-E_F\right), \end{aligned} \tag{10}$$

can be derived. Here the Fermi level and transport energy are denoted respectively by E_F and E_{tr}, the energy-dependent electrical conductivity or the differential conductivity $\sigma(E,E_F) = \left(-\frac{df}{dE}\right)\sigma(E) = qk_BTN(E,E_F)M(E,E_F)$ is comprised of the product of the energy distribution of conducting states ($N(E,E_F)$) and the energy distribution of mobility ($M(E,E_F)$), which integrates to

$$N(E_F) = \frac{\partial p}{\partial E_F} = \int dE\left(-\frac{df}{dE}\right)DOS(E), \tag{11}$$

and,

$$\mu(E_F) = \frac{q}{k_BT}\frac{\int dE\left(-\frac{df}{dE}\right)\sigma(E)}{\int dE\left(-\frac{df}{dE}\right)DOS(E)}, \tag{12}$$

to give respectively the conducting carrier density (or the effective density-of-states at the Fermi level) and the effective carrier mobility (or carrier mobility calculated for a given value of E_F). The carrier concentration (or carrier density) is calculated using the new electronic ground state formed upon IR light excitation ($\nu_0 = \epsilon_1 \propto -|g^2_{\omega_0}|/\omega_0$) and is given by $p = \int dE\ DOS(E)(1-f(E-\nu_0))$, where $f(E-E_0)$ is the Fermi function. $\sigma(E) = \pi^2\ tr\ \langle\langle\hat{\rho}(E)\rangle\ \hat{J}\ \langle\hat{\rho}(E)\rangle\ \hat{J}\rangle$ is the current-current correlation function, and $\hat{J} = iq\ \Sigma_j\left[J - g_{\omega_s}\left(\hat{a}^\dagger_{j+1}+\hat{a}_{j+1}-\hat{a}^\dagger_j-\hat{a}_j\right)\right]\left(\hat{c}^\dagger_i\hat{c}_j-\hat{c}^\dagger_j\hat{c}_i\right)$ is the current-current operator.[70–72] Unless otherwise stated, throughout our calculations we set $\hbar = 1$, $k_B = 1$ and express all energies in units of the transfer integral J ($= 143$ meV for rubrene).

3 Results

Fig. 1 summarizes the results of our calculations for (a) the DOS, (b) the carrier mobility, and (c) the thermoelectric PF in the absence (gray dotted line) and presence (blue solid line) of IR stimulation having field intensities $\langle I\rangle \propto N_{ph} = 35$. Corresponding plots of the DOS and the vibrational state shifting as a function of IR intensity are presented in Fig. 2 (a) and (b), along with plots of $N(E_F)$ and $\mu(E_F)$ as a function of both fixed Fermi level position and variable IR light intensity shown in Fig. 2 (c) and (d).

3.1 Resonant power factor enhancement in the DOS tail

As shown in Fig. 1 (a) and (b), as N_{ph} is increased to augment the coupling of IR light to intramolecular C-C stretching vibrations, pseudo-Jahn-Teller (PJT) distortions caused by stimulation of these intramolecular vibration modes lead to sharp peaks and enhanced mobility (μ) in the tail of the DOS. As a result, the thermoelectric power factor is resonantly enhanced (by a factor > 5) for values of the Fermi level (in the tail) that correspond to a practical range of carrier concentrations that is accessible by traditional chemical parts-per-million (ppm) doping techniques (e.g., $p \sim p_{intri.}$) as well as defect-free doping in a field-effect geometry, as shown in Fig. 1 (c). A third PF maximum occurs at very high carrier concentration ($p \gg p_{intri.}$) in the absence of the IR light stimulation (grey dotted line). However, the carrier concentration for this peak is far outside of the range attainable by traditional chemical doping techniques used in thermoelectric optimization (i.e., ppm chemical doping $\sim 1\times10^{-4}$ to 5×10^{-4} MR) or electrical doping in field-effect geometries ($\sim 5\times10^{-4}$ to 2×10^{-3} MR), as discussed elsewhere.[39] Here, MR is the unit of carrier concentration expressed in molar ratio. Conversely, while interfacial doping techniques such as EDLT-doping could be leveraged to reach carrier concentrations ($\sim 2\times10^{-3}$ to 3×10^{-1} MR) where PF is maximized in the absence of IR light,[46,73] EDLT-doping (and OFET-doping) are not bulk doping techniques and are therefore not as readily applicable to traditional thermoelectric device optimization schemes.[73,74]

3.2 DOS peak formation and mobility enhancement

This resonant enhancement of thermoelectric PF occurs via a resonant four-step intramolecular charge transfer process that couples ground state carriers (within the band) to excited state carriers (within the DOS tail), establishing a new electronic ground state within the DOS tail that is approximately $E_p \propto |g^2_{\omega_0}|/\omega_0$ from the unperturbed HOMO band edge as shown in Fig. 2 (a). Once in the new electronic ground state (ν_0) formed when $N_{ph} = 1$, the electronic system undergoes subsequent excitation to higher-lying ν_n states, moving ν_0 further into the tail and simultaneously opening up new transport channels within the tail DOS at $E = \nu_0$ and at energy multiples of the intramolecular vibration frequency as indicated in the vibrational state energy diagram of Fig. 2 (b). Further increasing N_{ph} to $N_{ph,crit.} = 25$

causes a lowering of the energies of both the electronic ground state (ν_0) and the first excited state (ν_1), at which point the threshold for a direct transition from the ν_0 ground state to the ν_2 excited state is reached. At this critical threshold photon number ($N_{ph,crit.} = 25$), the ν_1 and ν_2 DOS peaks converge asymptotically to form a quasi-delocalized band of states of considerably improved carrier degeneracy. As a result, both N and μ are shown to exhibit peaked behaviors as a function of N_{ph} as the ν_1 and ν_2 DOS peaks are symmetrically distributed relative to E_F (i.e., at the center of the bifurcation gap shown in Fig. 2 (b)). See Fig. S3 (a)-(b) for corresponding plots of the predicted Seebeck coefficient and electrical conductivity when the Fermi level is positioned at the center of the bifurcation gaps. However, unlike N, which is more strongly dependent on the degeneracy of states that are in close proximity of the Fermi level, the carrier mobility exhibits a broader dependence on N_{ph} due to enhanced carrier delocalization in this region (i.e., $\ell > a$, where ℓ is the carrier localization length and a is the lattice constant), and is shown in Fig. 2 (d) to taper off more slowly in the $N_{ph} \to \infty$ limit than for the predicted values of N. This is because while valence carrier redistribution to lower-lying electronic states becomes strongly suppressed in the $N_{ph} \to \infty$ limit, subsequent carrier redistribution into a higher-lying ν_n state causes carriers in the DOS tail to experience a progressively more delocalized energy landscape (i.e., $\ell \gg a$) than for a lower-lying ν_n state (which has $\ell \sim a$).

3.3 Mechanism of resonant power factor enhancement

The typical strategy to maximize thermoelectric PF in a material with a sharp feature in its energy-dependent DOS or mobility is to place the Fermi level $\sim 2.4k_BT$ away from the feature and thus maximize asymmetry in the energy distribution of conducting carriers $\sigma(E)$ with respect to E_F. However, given the behaviors of $DOS(E)$ and $\mu(E_F)$ near the critical cross-over points between the ν_1 and the ν_2 branches of the vibrational state energy diagram described above, it is apparent from Fig. 1 (a) and 2 (a) that while sharp features may occur in the DOS tails of weakly bonded materials upon the stimulation of IR-active vibrational modes, not all of them lead to a substantial enhancement of the thermoelectric PF.

This complexity in optimizing PF can be illustrated by assessing the asymmetries of the DOS and the carrier mobility within the Fermi window (shown in Fig. 3 (a)), which illustrate how resonant enhancements of N and μ (shown in Fig. 2 (c) and (d)) dictate the optimization of S and σ for maximum PF.[64] As shown in Fig. 3 (a), as the Fermi level is kept at its intrinsic position ($E_F = E_{F,intri.}$) and N_{ph} is increased from 25 to 35 to shift the ν_2 DOS peak (and thus the energy distribution of conducting carriers) from the top edge of the Fermi window ($+2.4k_BT$) to the bottom edge ($-2.4k_BT$), the resonant DOS peak shifts further away from $E = E_{F,intri.}$, bolstering asymmetries in the energy distribution of conducting carriers by causing states in the lower half of the intrinsic Fermi window ($E_F - 2.4k_BT < E < E_F$) to have markedly higher mobility than states in the upper half of the Fermi window ($E_F < E < E_F + 2.4k_BT$) as shown in Fig. 1 (b). Note that the states in the lower half of the Fermi window have high mobility because the ν_2 and ν_3 DOS peaks converge there ($\Delta_{peak} \sim k_BT$) while the states in the upper half of the Fermi window have low mobility because the ν_0 and ν_1 DOS peaks diverge there ($\Delta_{peak} \sim \hbar\omega_0 \gg k_BT$). As a result, S becomes optimized when the DOS peak is approximately $-2.4k_BT$ away from the intrinsic Fermi level position, exhibiting a linear dependence with N_{ph} in the very small photon number range spanning $25 < N_{ph} < 45$, and a sign change for larger values of N_{ph}, consistent with subsequent redistribution of valence carriers into higher-lying ν_n states. At the same time, since both N and μ are dramatically enhanced at the intrinsic Fermi level position when IR light is on (as shown in Figs. 1 and 2), the electrical conductivity is resonantly enhanced. Together this optimization of the Seebeck coefficient and enhancement of the electrical conductivity lead to a considerably improved thermoelectric PF in tail states when $N_{ph} = 35$. Conversely, for $N_{ph} > 35$, the DOS peaks on either side of the intrinsic Fermi window region asymptote to an energy that place them outside of the Fermi window, and they therefore do not induce modifications in S and σ that also optimize PF.

4 Discussion

This interplay between the shifting of the ν_2 DOS peak and consequent modifications in the behaviors of both $DOS(E)$ and $\mu(E_F)$ within the Fermi window brings about improvements in PF that cannot be readily explained by conventional photogeneration of carriers via the photo-Seebeck effect or the optical generation of Holstein small polarons. This is because while light absorption by the photo-Seebeck effect has previously been used to modify both the charge and thermoelectric transport properties of materials,[60,61,75] such methods are typically based on direct photogeneration of carriers (i.e., photo-doping) and differ from this approach, which utilizes light coupling to a particular vibrational mode to create sharply peaked DOS distortions in several regions of the DOS tail. Likewise, while the optical generation of photocarriers via the indirect stimulation of Holstein small polarons have also been shown to generate similar sharply peaked features in the DOS tail that lower the ground state energy of the electronic system,[38,50–52,54,55] such methods typically do not maximize asymmetries in the energy distribution of conducting carriers (ESI Note 5). DOS peaks created by PJT distortions, on the other hand, are shown in this work to evolve in such a way under optical excitation that they converge on one side of the Fermi window (with $\Delta_{peak} \sim k_BT$) to create a region of carrier energies with high mobility and diverge on the other side of the Fermi window ($\Delta_{peak} \sim \hbar\omega_0 \gg k_BT$) to create a region of carrier energies with relatively low mobility. Combined with the sharp changes in N, this modification in the behavior of the carrier mobility leads to a strong asymmetry in the energy distribution of conducting carriers and therefore high PF.

The mechanism of resonant power factor enhancement described in this work is therefore to be interpreted on the ground of the above novel, yet broadly generalizable class of resonant type$-\nu_{n\to n+2}$ pseudo-Jahn-Teller electronic transitions, which has its advantages in that it allows for the engineering of resonant enhancements of PF at both degenerate and non-degenerate

carrier concentrations, provided that the cavity photons (N_{ph}) or the intensity of IR light is precisely tuned to facilitate a resonant type$-\nu_{n\rightarrow n+2}$ transition into a shallower or a deeper energy level. Furthermore, since the modified ground state of the perturbed electronic system resulting from this interplay between redistributed carriers and molecular vibrations is shown to be effectively lowered by ~ 240 meV by the IR light interaction, the ionization potential of the material becomes considerably reduced, making these enhancements accessible to practical range of doping concentrations accessible by many p-type molecular dopants.[76] Together, this flexibility over tuning N_{ph} (and thus the asymmetries in the energy distribution of conducting carriers and the ionization potential of the material) provides a promising route for dramatically improving thermoelectric performance, especially within the technologically appealing class of weakly-bonded (soft) organic materials that is often characterized by low lattice thermal conductivity, but faces challenges when it comes to optimizing PF due to dopant limitations that are exacerbated in the presence of dynamic disorder.[39]

In addition to enabling enhancement of the thermoelectric PF at both degenerate and non-degenerate carrier concentrations, this method utilizing vibrational mode-selective DOS distortions provides the means for optimizing the temperature at which this enhancement occurs. There are two considerations in tuning the temperature dependence of the enhancement. First, as temperature increases, the DOS peaks broaden (Fig. 4 (a)), thereby reducing asymmetry in the energy distribution of conducting carriers relative to E_F. Second, as temperature increases, the Fermi window gets wider, causing more DOS peaks to span the $\pm 2.4k_BT$ domain of the Fermi window. While both effects are shown in Fig. 4 (a) to (c) to be particularly detrimental to thermoelectric performance for the intramolecular vibration frequency considered in this work, it follows from the above discussion that if DOS peaks are engineered to be further apart, while allowing for high mobility and low mobility regions to coexist on opposite sides of the Fermi window (as described above), large asymmetries in the energy distribution of conducting carriers could also be engineered to occur at a higher temperature ($T > 300$ K). The challenge, however, remains that in order to realize such enhancement of the thermoelectric PF, intramolecular vibrations with larger energies (and therefore larger peak spacings) would have to be considered. Nevertheless, since coupling valence carriers in weakly-bonded materials to higher energy intramolecular vibration modes ($\hbar\omega_0 > 2J \sim 3000$ K) can under certain conditions oxidize the material,[20,42,77] break bonds,[78,79] or mix vibrational modes,[80–83] additional strategies to mitigate these possibilities may need to be implemented to take advantage of these DOS distortions for high-temperature TE applications.

In this work we consider the explicit coupling of valence carriers to IR-active intramolecular vibrations and approximate the effects of intermolecular interactions (e.g., acoustic phonon scattering) by mapping the electronic problem onto an thermalized phonon bath governed by Peierls intermolecular electron-phonon interactions (which dictate the broadening of the Dirac-delta DOS peaks). Intermolecular interactions,[81,82] such as those arising from the direct application of strain[83] or the engineering of supramolecular interactions,[84] could however alter the positioning and broadening of DOS peaks and therefore the optimal value of PF. Strain effects in soft materials, for example, are known to induce work function variation[85] and vibrational frequencies shifts,[86] and have been used to modulate the strength of the electron-phonon coupling (and thus, in the context of this work, the number of carriers that are redistributed to excited states).[83] Because intermolecular interactions may impact molecular arrangements and symmetries,[86–89] a robust incorporation of their effects in predicting vibrational mode-selective PF enhancements may require a detailed study of the full phonon dispersion[81–83] or experimental measurements of strain effects.

Conclusions

We have developed a model that accounts for the effects of mode-selective molecular vibrations, induced via the direct application of IR light, on the thermoelectric properties of a prototypical soft organic material. Vibrational coupling induces a resonant enhancement in the bi-exponential tail region of carrier density-of-states that is most accessible to practical doping strategies for such materials. As the the number of photons that couples to C-C stretching vibrations is increase from $N_{ph} = 15$ to $N_{ph} = 35$, pseudo-Jahn-Teller distortions, caused by a lowering of the energy and the symmetry of the electronic ground state, create sharp peaks in the DOS tail that merges on the lower side of the Fermi level ($E_F - 2.4k_BT < E < E_F$) and diverges on the upper of the Fermi level ($E_F < E < E_F + 2.4k_BT$) to maximize the asymmetries in the energy distribution of conducting carriers. These peaks provide enhancements in carrier mobility and thermoelectric PF for a range of carrier concentrations corresponding to locations of the Fermi level in the tail, and is physically distinct from the scenario of the direct photogeneration of free carriers by the Photo-Seebeck effect or the indirect photogeneration of carriers via small polaron formation. Thus, while the interaction of light with matter has been traditionally interpreted in the thermoelectric context as a method to dope TE materials, here we find that it can also be used to create resonant impurity states akin to those that occur in traditional high-performance TE material in which resonant dopant impurities are introduced to resonantly enhance $DOS(E)$ (e.g., thallium-doped lead telluride). Additional design considerations involving the engineering of intermolecular interactions and their associated vibration modes may have to be developed in order to take advantage of these resonant DOS distortions for maximum power factor enhancement in tail states.

Author Contributions

S.W.B. performed the research, developed the computational framework, and wrote the paper. S.W.B. and K.P.P. conceptualized the research and analyzed the model results. K.P.P. assisted with writing the paper.

Conflicts of interest

Authors declare no competing interests.

Acknowledgements

This material is based upon work supported by the National Science Foundation Graduate Research Fellowship Program under Grant No. DGE 1256260.

Notes and references

1 M. S. Dresselhaus, G. Chen, M. Y. Tang, R. G. Yang, H. Lee, D. Z. Wang, Z. F. Ren, J.-P. Fleurial and P. Gogna, *Advanced Materials*, 2007, **19**, 1043–1053.

2 L. D. Hicks and M. S. Dresselhaus, *Physical Review B*, 1993, **47**, 16631–16634.

3 L. D. Hicks and M. S. Dresselhaus, *Physical Review B*, 1993, **47**, 12727–12731.

4 J. Mao, Z. Liu and Z. Ren, *npj Quantum Materials*, 2016, **1**, 16028.

5 V. A. Kulbachinskii, N. B. Brandt, P. A. Cheremnykh, S. A. Azou, J. Horak and P. Lošták, *physica status solidi (b)*, 1988, **150**, 237–243.

6 V. Kulbachinskii, H. Negishi, M. Sasaki, Y. Giman, M. Inoue, P. Lostak and J. Horak, *physica status solidi (b)*, 1997, **199**, 505–513.

7 M. K. Zhitinskaya, S. A. Nemov and Y. I. Ravich, *Physics of the Solid State*, 1998, **40**, 1098–1100.

8 B. Wiendlocha, *Journal of Electronic Materials*, 2016, **45**, 3515–3531.

9 J. P. Heremans, V. Jovovic, E. S. Toberer, A. Saramat, K. Kurosaki, A. Charoenphakdee, S. Yamanaka and G. J. Snyder, *Science*, 2008, **321**, 554–557.

10 J. P. Heremans, B. Wiendlocha and A. M. Chamoire, *Energy Environ. Sci.*, 2012, **5**, 5510–5530.

11 A. Majumdar, *Science*, 2004, **303**, 777–778.

12 G. D. Mahan and J. O. Sofo, *Proceedings of the National Academy of Sciences*, 1996, **93**, 7436–7439.

13 T. E. Humphrey and H. Linke, *Phys. Rev. Lett.*, 2005, **94**, 096601.

14 J. Xin, Y. Tang, Y. Liu, X. Zhao, H. Pan and T. Zhu, *npj Quantum Materials*, 2018, **3**, 9.

15 P. Norouzzadeh and D. Vashaee, *Scientific Reports*, 2016, **6**, 22724.

16 P. Giraldo-Gallo, P. Walmsley, B. Sangiorgio, S. C. Riggs, R. D. McDonald, L. Buchauer, B. Fauqué, C. Liu, N. A. Spaldin, A. Kaminski, K. Behnia and I. R. Fisher, *Phys. Rev. Lett.*, 2018, **121**, 207001.

17 G. D. Scholes, *ACS NaNo*, 2008, **2**, 523–537.

18 O. Tal, Y. Rosenwaks, Y. Preezant, N. Tessler, C. K. Chan and A. Kahn, *Phys. Rev. Lett.*, 2005, **95**, 256405.

19 L. Goris, K. Haenen, M. Nesládek, P. Wagner, D. Vanderzande, L. De Schepper, J. D'haen, L. Lutsen and J. V. Manca, *Journal of Materials Science*, 2005, **40**, 1413–1418.

20 C. Krellner, S. Haas, C. Goldmann, K. P. Pernstich, D. J. Gundlach and B. Batlogg, *Physical Review B*, 2007, **75**, 245115.

21 X. Ren, M. J. Bruzek, D. A. Hanifi, A. Schulzetenberg, Y. Wu, C.-H. Kim, Z. Zhang, J. E. Johns, A. Salleo, S. Fratini, A. Troisi, C. J. Douglas and C. D. Frisbie, *Advanced Electronic Materials*, 2017, **3**, 1700018.

22 P. J. Diemer, J. Hayes, E. Welchman, R. Hallani, S. J. Pookpanratana, C. A. Hacker, C. A. Richter, J. E. Anthony, T. Thonhauser and O. D. Jurchescu, *Advanced Electronic Materials*, 2017, **3**, 1600294.

23 M. Knupfer, M. Merkel, M. S. Golden, J. Fink, O. Gunnarsson and V. P. Antropov, *Phys. Rev. B*, 1993, **47**, 13944–13947.

24 A. A. Bakulin, A. Rao, V. G. Pavelyev, P. H. M. van Loosdrecht, M. S. Pshenichnikov, D. Niedzialek, J. Cornil, D. Beljonne and R. H. Friend, *Science*, 2012, **335**, 1340–1344.

25 A. a. Bakulin, R. Lovrincic, X. Yu, O. Selig, H. J. Bakker, Y. L. a. Rezus, P. K. Nayak, A. Fonari, V. Coropceanu, J.-L. Brédas and D. Cahen, *Nature Communications*, 2015, **6**, 7880.

26 F. Bussolotti, J. Yang, T. Yamaguchi, K. Yonezawa, K. Sato, M. Matsunami, K. Tanaka, Y. Nakayama, H. Ishii, N. Ueno and S. Kera, *Nature Communications*, 2017, **8**, year.

27 J. Nitta, K. Miwa, N. Komiya, E. Annese, J. Fujii, S. Ono and K. Sakamoto, *Scientific Reports*, 2019, **9**, 9645.

28 S. Duhm, Q. Xin, S. Hosoumi, H. Fukagawa, K. Sato, N. Ueno and S. Kera, *Advanced Materials*, 2012, **24**, 901–905.

29 Y. Nakayama, S. Kera and N. Ueno, *Journal of Materials Chemistry C*, 2020, **8**, 9090–9132.

30 E. Janzén, R. Stedman, G. Grossmann and H. G. Grimmeiss, *Phys. Rev. B*, 1984, **29**, 1907–1918.

31 M. V. Limaye, S. C. Chen, C. Y. Lee, L. Y. Chen, S. B. Singh, Y. C. Shao, Y. F. Wang, S. H. Hsieh, H. C. Hsueh, J. W. Chiou, C. H. Chen, L. Y. Jang, C. L. Cheng, W. F. Pong and Y. F. Hu, *Scientific Reports*, 2015, **5**, 11466.

32 C. H. Crouch, J. E. Carey, M. Shen, E. Mazur and F. Y. Génin, *Applied Physics A*, 2004, **79**, 1635–1641.

33 A. Luque, A. Martí, E. Antolín and C. Tablero, *Physica B: Condensed Matter*, 2006, **382**, 320–327.

34 E. Ertekin, M. T. Winkler, D. Recht, A. J. Said, M. J. Aziz, T. Buonassisi and J. C. Grossman, *Phys. Rev. Lett.*, 2012, **108**, 026401.

35 M. T. Winkler, D. Recht, M.-J. Sher, A. J. Said, E. Mazur and M. J. Aziz, *Phys. Rev. Lett.*, 2011, **106**, 178701.

36 D. Polak, R. Jayaprakash, T. P. Lyons, L. Martínez-Martínez, A. Leventis, K. J. Fallon, H. Coulthard, D. G. Bossanyi, K. Georgiou, A. J. Petty, J. Anthony, H. Bronstein, J. Yuen-Zhou, A. I. Tartakovskii, J. Clark and A. J. Musser, *Chemical Science*, 2020, **11**, 343–354.

37 C.-Y. Cheng, R. Dhanker, C. L. Gray, S. Mukhopadhyay, E. R. Kennehan, J. B. Asbury, A. Sokolov and N. C. Giebink, *Physical Review Letters*, 2018, **120**, 017402.

38 R. Osterbacka, C. P. An, X. M. Jiang and Z. V. Vardeny, *Science*, 2000, **287**, 839–842.

39 S. W. Birch and K. P. Pipe, *Journal of Applied Physics*, 2022, **131**, 135104.

40 S. Yogev, R. Matsubara, M. Nakamura, U. Zschieschang, H. Klauk and Y. Rosenwaks, *Physical Review Letters*, 2013, **110**, 1–5.

41 G. Garcia-Belmonte, P. P. Boix, J. Bisquert, M. Sessolo and H. J. Bolink, *Solar Energy Materials and Solar Cells*, 2010, **94**,

366–375.
42 W. L. Kalb, S. Haas, C. Krellner, T. Mathis and B. Batlogg, *Physical Review B*, 2010, **81**, 155315.
43 H. N. Chern, C. L. Lee and T. F. Lei, *IEEE Transactions on Electron Devices*, 1994, **41**, 698–702.
44 F. Djamdji, P. LeComber, R. Schumacher, P. Thomas and K. Weber, *Journal of Non-Crystalline Solids*, 1987, **97-98**, 543–546.
45 D. Monroe and M. A. Kastner, *Phys. Rev. B*, 1986, **33**, 8881–8884.
46 F. Zhang, Y. Zang, D. Huang, C. A. Di, X. Gao, H. Sirringhaus and D. Zhu, *Advanced Functional Materials*, 2015, **25**, 3004–3012.
47 S. Olthof, S. Mehraeen, S. K. Mohapatra, S. Barlow, V. Coropceanu, J.-L. Brédas, S. R. Marder and A. Kahn, *Physical Review Letters*, 2012, **109**, 176601.
48 T. Menke, D. Ray, H. Kleemann, K. Leo and M. Riede, *physica status solidi (b)*, 2015, **252**, 1877–1883.
49 M. L. Tietze, P. Pahner, K. Schmidt, K. Leo and B. Lüssem, *Advanced Functional Materials*, 2015, **25**, 2701–2707.
50 S. Swain, *Journal of Physics A: Mathematical, Nuclear and General*, 1973, **6**, 192–204.
51 M. Cini and A. D'Andrea, *Journal of Physics C: Solid State Physics*, 1988, **21**, 193–235.
52 A. D'Andrea, *Physical Review A*, 1989, **39**, 5143–5152.
53 J. Ranninger, *Phys. Rev. B*, 1993, **48**, 13166–13169.
54 S. Ciuchi, F. de Pasquale and D. Feinberg, *Europhysics Letters (EPL)*, 1995, **30**, 151–156.
55 S. Ciuchi, F. de Pasquale, S. Fratini and D. Feinberg, *Physical Review B*, 1997, **56**, 4494–4512.
56 S. Ciuchi and S. Fratini, *Physical Review Letters*, 2011, **106**, 1–4.
57 E. V. Korovkin and R. K. Nikolaev, *Physics of the Solid State*, 1999, **41**, 1015–1016.
58 L. Zuppiroli, A. Bieber, D. Michoud, G. Galli, F. Gygi, M. Bussac and J. André, *Chemical Physics Letters*, 2003, **374**, 7–12.
59 A. S. Alexandrov and J. Ranninger, *Phys. Rev. B*, 1992, **45**, 13109–13112.
60 J. Tauc, *Czechoslovak Journal of Physics*, 1955, **5**, 528–535.
61 H. B. Kwok and R. H. Bube, *Journal of Applied Physics*, 1973, **44**, 138–144.
62 F. Bussolotti, J. Yang, M. Hiramoto, T. Kaji, S. Kera and N. Ueno, *Physical Review B*, 2015, **92**, 115102.
63 H. Fritzsche, *Solid State Communications*, 1971, **9**, 1813–1815.
64 M. Cutler and N. F. Mott, *Physical Review*, 1969, **181**, 1336–1340.
65 S. Swain, *Journal of Physics A: Mathematical, Nuclear and General*, 1973, **6**, L169–L173.
66 G. D. Mahan, *Phys. Rev.*, 1967, **163**, 612–617.
67 B. I. Lundqvist, *Physik der kondensierten Materie*, 1967, **6**, 193–205.
68 D. C. Langreth, *Phys. Rev. B*, 1970, **1**, 471–477.
69 M. Cini, *Phys. Rev. B*, 1978, **17**, 2486–2493.
70 S. Fratini and S. Ciuchi, *Physical Review Letters*, 2009, **103**, 266601.
71 S. Ciuchi and S. Fratini, *Physical Review B*, 2012, **86**, 245201.
72 M. Capone, W. Stephan and M. Grilli, *Physical Review B*, 1997, **56**, 4484–4493.
73 H. Tanaka, K. Kanahashi, N. Takekoshi, H. Mada, H. Ito, Y. Shimoi, H. Ohta and T. Takenobu, *Science Advances*, 2020, **6**, eaay8065.
74 H. Ohta, T. Mizuno, S. Zheng, T. Kato, Y. Ikuhara, K. Abe, H. Kumomi, K. Nomura and H. Hosono, *Advanced Materials*, 2012, **24**, 740–744.
75 J. G. Harper, H. E. Matthews and R. H. Bube, *Journal of Applied Physics*, 1970, **41**, 3182–3184.
76 J. Li, I. Duchemin, O. M. Roscioni, P. Friederich, M. Anderson, E. Da Como, G. Kociok-Köhn, W. Wenzel, C. Zannoni, D. Beljonne, X. Blase and G. D'Avino, *Mater. Horiz.*, 2019, **6**, 107–114.
77 T. Zimmerling, K. Mattenberger, M. Döbeli, M. J. Simon and B. Batlogg, *Phys. Rev. B*, 2012, **85**, 134101.
78 C. H. Wang, S. W. Chen and J. Hwang, *Applied Physics Letters*, 2009, **95**, 103302.
79 J. Zhang, G. F. S. Whitehead, T. D. Manning, D. Stewart, C. I. Hiley, M. J. Pitcher, S. Jansat, K. Prassides and M. J. Rosseinsky, *Journal of the American Chemical Society*, 2018, **140**, 18162–18172.
80 A. Girlando, L. Grisanti, M. Masino, I. Bilotti, A. Brillante, R. G. Della Valle and E. Venuti, *Physical Review B - Condensed Matter and Materials Physics*, 2010, **82**, 1–8.
81 G. Schweicher, G. D'Avino, M. T. Ruggiero, D. J. Harkin, K. Broch, D. Venkateshvaran, G. Liu, A. Richard, C. Ruzié, J. Armstrong, A. R. Kennedy, K. Shankland, K. Takimiya, Y. H. Geerts, J. A. Zeitler, S. Fratini and H. Sirringhaus, *Advanced Materials*, 2019, **31**, 1902407.
82 T. F. Harrelson, V. Dantanarayana, X. Xie, C. Koshnick, D. Nai, R. Fair, S. A. Nuñez, A. K. Thomas, T. L. Murrey, M. A. Hickner, J. K. Grey, J. E. Anthony, E. D. Gomez, A. Troisi, R. Faller and A. J. Moulé, *Materials Horizons*, 2019, **6**, 182–191.
83 M. T. Ruggiero, S. Ciuchi, S. Fratini and G. D'Avino, *The Journal of Physical Chemistry C*, 2019, **123**, 15897–15907.
84 G. R. Desiraju, *Journal of the American Chemical Society*, 2013, **135**, 9952–9967.
85 Y. Wu, A. R. Chew, G. a. Rojas, G. Sini, G. Haugstad, A. Belianinov, S. V. Kalinin, H. Li, C. Risko, J.-L. Brédas, A. Salleo and C. D. Frisbie, *Nature Communications*, 2016, **7**, 10270.
86 A. Kelley, *Condensed-Phase Molecular Spectroscopy and Photophysics*, Wiley, 2012.
87 L. Qi and D. C. Chrzan, *Phys. Rev. Lett.*, 2014, **112**, 115503.
88 M. Asher, D. Angerer, R. Korobko, Y. Diskin-Posner, D. A. Egger and O. Yaffe, *Advanced Materials*, 2020, **32**, 1908028.
89 O. Delaire, J. Ma, K. Marty, A. F. May, M. A. McGuire, M.-H. Du, D. J. Singh, A. Podlesnyak, G. Ehlers, M. D. Lumsden and B. C. Sales, *Nature Materials*, 2011, **10**, 614–619.

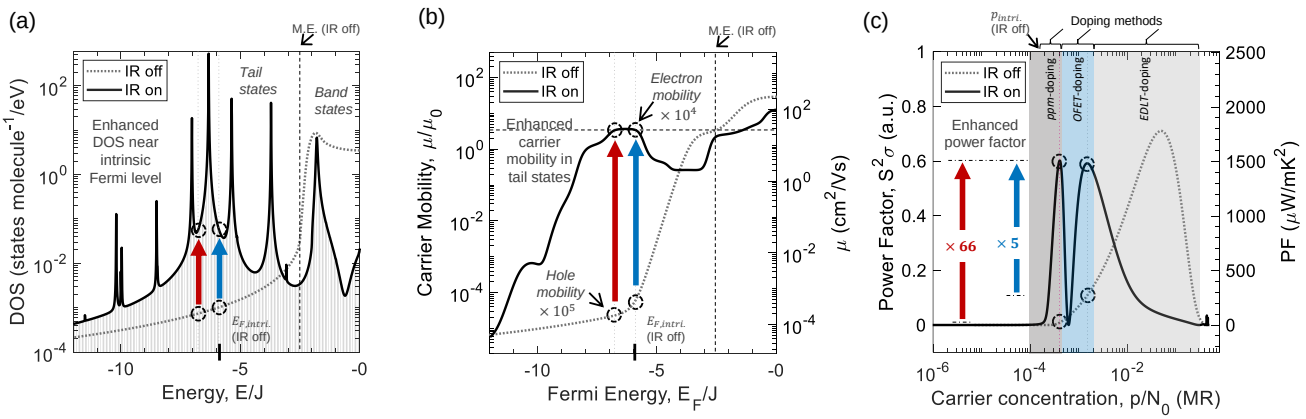

Fig. 1 Resonant photoenhancement of the thermoelectric PF. Calculated modification of (a) carrier DOS, (b) carrier mobility (μ), and (c) thermoelectric power factor upon coupling of incident IR radiation to an intramolecular vibrational mode of the prototypical soft organic material, rubrene. All energies are expressed in units of the transfer integral ($J = 143$ meV), and mobility in units of $\mu_0 = 7$ cm^2/Vs. The red and blue arrows indicate enhancements in $DOS(E)$, $\mu(E_F)$ and PF measured relative to the case when IR light is off (dark grey dotted line), and when the Fermi level position is $\pm 2.4\ k_BT$ from the most strongly peaked Dirac-delta-like resonance at $E = 6.33J$ [c.f. Fig. 1 (a)]. Note that the resonant PF enhancement that occurs on the $+2.4k_BT$ side of this resonant peak (indicated by blue arrow in Fig. 1 (c)), lies very close to the intrinsic Fermi level position for the case when $N_{ph} = 35$, and is therefore accessible by both chemical parts-per-million (ppm) doping [47–49] or defect-free doping in organic field-effect transistor (OFET) geometry. [46]

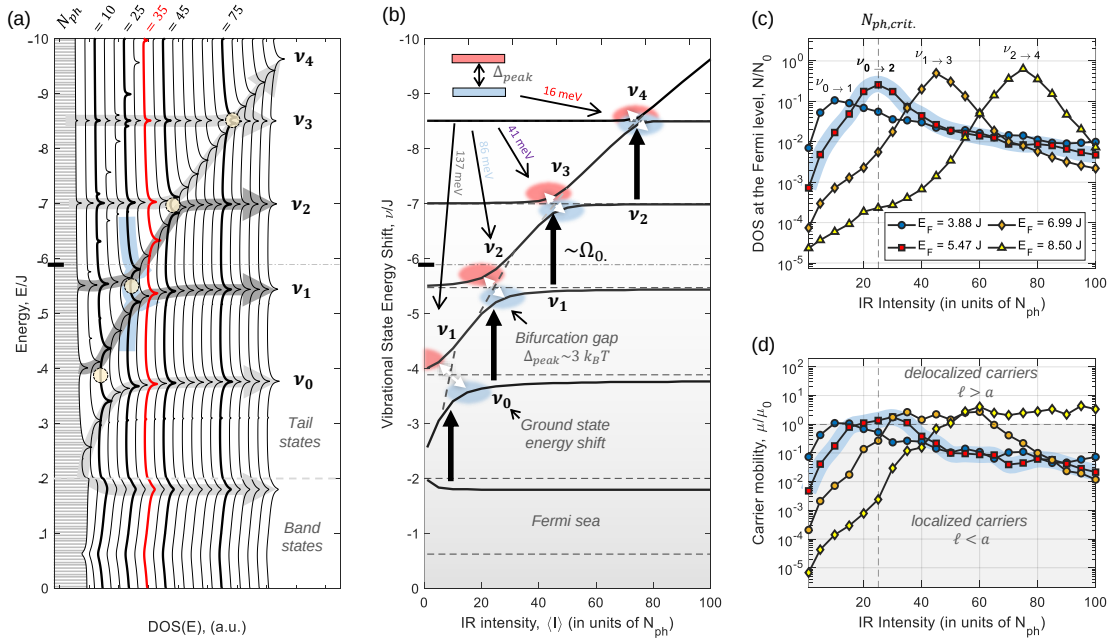

Fig. 2 Mechanism of resonant power factor enhancement. (a)-(b). Calculated DOS showing the evolution of Dirac-delta-like resonances and the shifting of the ground and excited vibrational state energies as the IR intensity is increased from $N_{ph} = 1$ to $N_{ph} = 50$ (with increments of 5) to facilitate the redistribution of valence carriers from band states to tail states. Several bifurcation gaps are shown to emerge in the plot of the vibrational state energy shifts ν vs. N_{ph} shown in Fig. 2 (b). These bifurcations occur at energy multiples of the stimulated intramolecular vibration frequency ω_0 and are interpreted as a symmetry-broken electronic ground state created upon the formation of a pseudo-Jahn Teller distortion. The evolution of N and μ as the IR intensity is increased to vary a DOS peak across all four of bifurcation points studied in this work is shown in Figs. 2 (c) and (d), respectively.

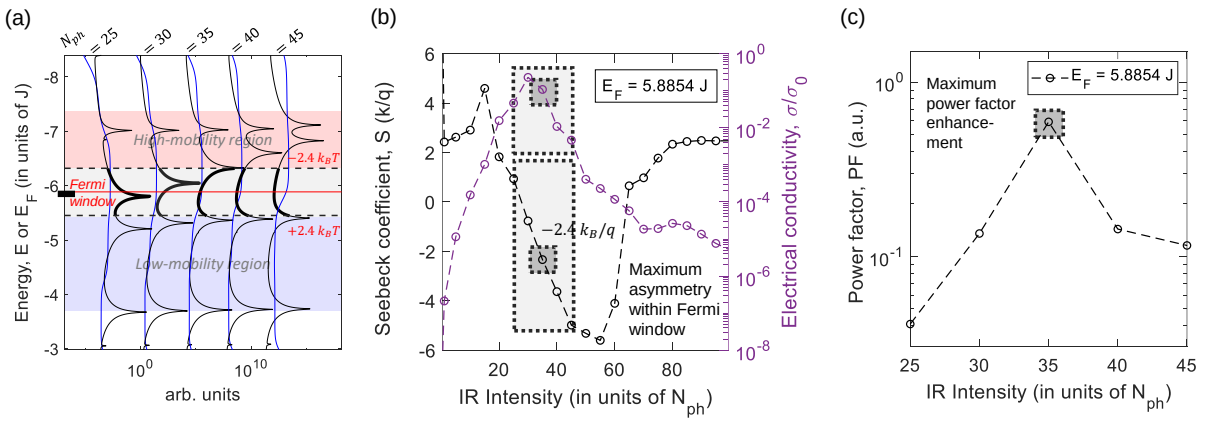

Fig. 3 Close-ups of the asymmetries in the energy distribution of conducting carriers. (a) Highlights of the DOS peak shifting (black lines) within the Fermi window showing how subtle changes in the behaviors of $DOS(E)$ and $\mu(E_F)$ maximize asymmetries in the energy distribution of conducting carriers when $N_{ph} = 35$. Corresponding plots for how the Seebeck coefficient, electrical conductivity, and the thermoelectric PF are modified as a result of this enhanced asymmetry in the energy distribution of conducting carriers are displayed in Fig. 3 (b) and (c), respectively, for values of N_{ph} between 25 and 45.

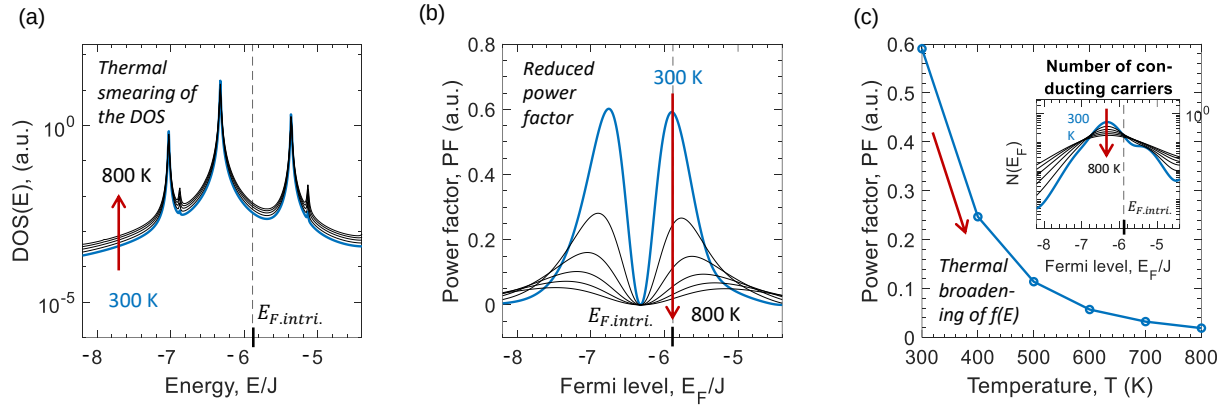

Fig. 4 Temperature dependence of Dirac-delta-like resonances for $T > 300$ K. (b) and (c) show that the thermoelectric PF predicted near the intrinsic Fermi level position declines considerably as temperature is increased, primarily due to a widening of the Fermi window to include more resonant peaks. Note that a higher energy vibrational resonance would lead to a greater peak spacing and hence greater performance at high temperatures. As shown in the inset of (c), the predicted reduction in PF doesn't appear to originate from the thermal broadening of the $DOS(E)$ shown in (a) since the values of $N(E_F)$ predicted to occur at the intrinsic Fermi level position are essentially the same for all temperatures $T > 300$ K examined in this work.